

# Concatenated continuous driving of silicon qubit by amplitude and phase modulation

Takuma Kuno,<sup>1, 2, \*</sup> Takeru Utsugi,<sup>1</sup> Andrew J. Ramsay,<sup>3</sup> Normann Mertig,<sup>3</sup> Noriyuki Lee,<sup>1</sup> Itaru Yanagi,<sup>1</sup> Toshiyuki Mine,<sup>1</sup> Nobuhiro Kusuno,<sup>1</sup> Hideo Arimoto,<sup>1</sup> Sofie Beyne,<sup>4</sup> Julien Jussot,<sup>4</sup> Stefan Kubicek,<sup>4</sup> Yann Canvel,<sup>4</sup> Clement Godfrin,<sup>4</sup> Bart Raes,<sup>4</sup> Yosuke Shimura,<sup>4</sup> Roger Loo,<sup>4, 5</sup> Sylvain Baudot,<sup>4</sup> Danny Wan,<sup>4</sup> Kristiaan De Greve,<sup>4, 6</sup> Shinichi Saito,<sup>1</sup> Digh Hisamoto,<sup>1</sup> Ryuta Tsuchiya,<sup>1</sup> Tetsuo Kodera,<sup>2</sup> and Hiroyuki Mizuno<sup>1</sup>

<sup>1</sup>Research and Development Group, Hitachi, Ltd., Kokubunji, Tokyo 185-8601, Japan

<sup>2</sup>Department of Electrical and Electronic Engineering,

Institute of Science Tokyo, Meguro, Tokyo 152-8552, Japan

<sup>3</sup>Hitachi Cambridge Laboratory, J. J. Thomson Ave., Cambridge, CB3 0HE, United Kingdom

<sup>4</sup>IMEC, 3001 Leuven, Belgium

<sup>5</sup>Department of Solid-State Sciences, Ghent University, Krijgslaan 285, 9000 Ghent, Belgium

<sup>6</sup>Department of Electrical Engineering (ESAT-MNS), KU Leuven, Leuven, Belgium

(Dated: January 19, 2026)

The rate of coherence loss is lower for a qubit under Rabi drive compared to a freely evolving qubit,  $T_2^{\text{Rabi}} > T_2^*$ . Building on this principle, concatenated continuous driving (CCD) keeps the qubit under continuous drive to suppress noise and manipulate dressed states by either phase or amplitude modulation. In this work, we propose a new variant of CCD which simultaneously modulates both the amplitude and phase of the driving field to generate a circularly-polarized field in the rotating frame of the carrier frequency. This circular-modulated (CM)-CCD cancels the counter-rotating term in the second rotating frame, eliminating a systematic pulse-area error that arises from an imperfect rotating wave approximation for fast gates. Numerical simulations demonstrate that the proposed CMCCD achieves higher gate fidelity than conventional CCD schemes. We further implement and compare different CCD protocols using an electron spin-qubit in an isotopically purified <sup>28</sup>Si-MOS quantum dot and evaluate its robustness by applying static detuning and Rabi frequency errors. The robustness is significantly improved compared to standard Rabi-drive, showing the effectiveness of this scheme for qubit arrays with variation in qubit frequency, coupling to Rabi drive, and low frequency noise. The proposed scheme can be applied to various physical systems, including trapped atoms, cold atoms, superconducting qubits, and NV-centers.

## I. INTRODUCTION

The long coherence time of a quantum state is an essential resource for quantum technologies, including quantum sensing and metrology [1–3], quantum simulations [4–6], and quantum computing [7, 8]. In particular, quantum computation requires the high-precision control of large-scale qubit arrays [9–11]. Low frequency noise can be considered as an uncertainty in the qubit frequency and drive field. Consequently, control methods that are tolerant to uncertainties are important. Furthermore, the inhomogeneity of the drive field and the variations of the qubit characteristics across the large-scale qubits pose significant challenges to achieving reliable qubit control.

Dressing of a two-level quantum state has been demonstrated to effectively extend coherence times in various quantum systems, including trapped atoms [12, 13], NV centers [14–16], silicon carbide divacancy [17], donor-based qubit in silicon [18], and hole-qubit in germanium [19]. In the dressed state, an electromagnetic driving field interacts resonantly with the quantum system and induces dynamical decoupling from noise, providing reliable control of the quantum states. Although this approach has the advantage of being robust against environmental noise, it remains vulnerable to fluctuations in the driving field. One approach to address this issue is the sinusoidally modulated, always rotating and

tailored (SMART) protocol, proposed in ref [20]. The SMART protocol utilizes the alternating phase of a sinusoidally amplitude modulated drive to reduce the impact of drive field fluctuations and the detuning error. The SMART protocol has been demonstrated using qubits in NV centers [21] and silicon quantum dots [22], and has recently been effective for the entangling gate operation [23]. Another strategy is concatenated continuous driving (CCD) scheme [24–31]. By modulating the microwave (MW) driving amplitude or phase, the CCD scheme engages the quantum states in the double-dressed state, decreasing sensitivity to the driving field fluctuations. The CCD scheme has recently been experimentally studied for the qubit application [32] and demonstrated gate fidelity improvement in noisy isotopically natural Si-MOS devices [33]. Since the double-dressed qubit requires control in the second rotating frame, the rotating wave approximation (RWA) is needed to cancel the counter-rotating term. However, the residual counter-rotating term can be an obstacle for precise qubit control, resulting in decreased gate fidelity.

In this work, we propose a variant of the CCD protocol. Unlike conventional methods, which employ either amplitude or phase modulation, our approach modulates both amplitude and phase simultaneously. This circular-modulated (CM)CCD cancels the counter-rotating field, resulting in a circular polarization driving field in the first rotating frame (Fig. 1). Consequently, in the second ro-

tating frame of the modulated drive, there is no residual second harmonic term to give rise to a systematic gate error on resonance. We experimentally demonstrate the proposed CMCCD using a spin-qubit in an isotopically enriched silicon quantum dot. The dependence of the chevron pattern on the modulation strength aligns well with simulations, confirming the accurate implementation of the CMCCD scheme. We also evaluate the robustness of CMCCD, amplitude-modulated (AM) and phase-modulated (PM) CCD, by artificially adding detuning and Rabi static errors in a relatively low-noise environment, demonstrating the increased robustness compared with the bare qubit. The proposed CMCCD scheme offers a promising solution that combines precise qubit control with enhanced robustness in the presence of environmental noise and variability in qubits or driving fields across large-scale qubits.

## II. CONCATENATED CONTINUOUS DRIVING BY AMPLITUDE AND PHASE MODULATION

Two primary methods of CCD protocols have been established: AMCCD and PMCCD. Both approaches enable the realization of robust qubits; however, they suffer from a fundamental limitation—errors arising from

the validity of the second RWA. The electron spin resonance mechanism is typically analyzed in the first rotating frame, where the co-rotating component of the linearly polarized microwave drive  $\omega_{\text{mw}}$  and the Larmor precession  $\omega_L$  of the spin results in a d.c drive field that drives a Rabi oscillation at frequency  $\Omega_0$ . The counter-rotating component gives rise to a second-harmonic term at  $2\omega_{\text{mw}}$ . The effect of the second harmonic on the spin dynamics integrates to zero, since  $\Omega_0/2\pi \sim 1-10$  MHz  $\ll \omega_{\text{mw}}/2\pi = 10 - 20$  GHz in the typical spin-qubit situation, which is known as the RWA.

For CCD control, the microwave drive is modulated, and in the first rotating frame, the modulation gives rise to an ac-field of amplitude  $\epsilon_m$ , and the Hamiltonian maps to the classic Rabi problem. Hence, the analysis makes a second rotating frame transformation at the Rabi frequency  $\Omega_0$ . However, the gate-speed is now determined by  $\epsilon_m$ , and setting  $\epsilon_m \ll \Omega_0$  would result in very slow operations. Hence, the non-negligible counter-rotating term results in a systematic pulse-area error on resonance. Since the RWA error stems from the use of linearly polarized driving fields, generating the circular polarization in the first rotating frame eliminates the counter-rotating term.

Building on this insight, we introduce a generalized formulation of CCD-drive as ( $\hbar = 1$ ):

$$H_{\text{lab}}(t) = \frac{\omega_L}{2}\sigma_z + (\Omega_0 + \Delta_\Omega) \left[ \cos\left(\omega_{\text{mw}}t + \phi_{\text{mw}} - \frac{2\alpha_P\epsilon_m}{\Omega_0} \sin(\Omega_0t - \theta_m)\right) \right. \\ \left. + \frac{2\alpha_A\epsilon_m}{\Omega_0} \sin(\Omega_0t - \theta_m) \sin\left(\omega_{\text{mw}}t + \phi_{\text{mw}} - \frac{2\alpha_P\epsilon_m}{\Omega_0} \sin(\Omega_0t - \theta_m)\right) \right] \sigma_x, \quad (1)$$

where  $\sigma_i (i \in \{x, y, z\})$  are Pauli matrices,  $\omega_L$  is the qubit Larmor frequency,  $\Omega_0$  is the Rabi frequency, and  $\Delta_\Omega$  is Rabi frequency error (Rabi error), caused by MW fluctuations or inhomogeneity. The MW drive is characterized by its frequency  $\omega_{\text{mw}}/2\pi$  and phase  $\phi_{\text{mw}}$ . Modulation parameters of CCD scheme is defined by modulation strength  $\epsilon_m$  and modulation phase  $\theta_m$ . Here, we introduce two dimensionless parameters: amplitude modulation ratio  $\alpha_A$  and phase modulation ratio  $\alpha_P$  ( $\alpha_A, \alpha_P \geq 0$ ,  $\alpha_A + \alpha_P = 1$ ). For AMCCD ( $\alpha_A = 1, \alpha_P = 0$ ) and PMCCD ( $\alpha_A = 0, \alpha_P = 1$ ), and the bare qubit corresponds to  $\alpha_A = \alpha_P = 0$ . As discussed below, if ampli-

tude and phase are equally modulated,  $\alpha_A = \alpha_P = 1/2$ , a circularly polarized drive field arises in the first rotating frame. We name this scheme circular-modulated CCD (CMCCD).

To demonstrate this, we move to the first rotating frame defined by the time-dependent Hamiltonian [28]

$$H_0^{(1)}(t) = \left[ \frac{\omega_{\text{mw}}}{2} - \alpha_P\epsilon_m \cos(\Omega_0t - \theta_m) \right] \sigma_z, \quad (2)$$

the rotating frame Hamiltonian becomes

$$H_{\text{rot}}^{(1)}(t) = -H_0^{(1)}(t) + e^{i \int_0^t H_0^{(1)}(t') dt'} H_{\text{lab}}(t) e^{-i \int_0^t H_0^{(1)}(t') dt'} \\ \approx \frac{\delta}{2}\sigma_z + \frac{\Omega_0 + \Delta_\Omega}{2}\sigma_{\phi_{\text{mw}}} - \left(1 + \frac{\Delta_\Omega}{\Omega_0}\right) \alpha_A\epsilon_m \sin(\Omega_0t - \theta_m) \sigma_{\phi_{\text{mw}+\pi/2}} + \alpha_P\epsilon_m \cos(\Omega_0t - \theta_m) \sigma_z,$$

where  $\delta/2\pi = (\omega_L - \omega_{\text{mw}})/2\pi$  is detuning and we define

$\sigma_\phi \equiv \cos(\phi)\sigma_x + \sin(\phi)\sigma_y$ . Here, we use the first RWA

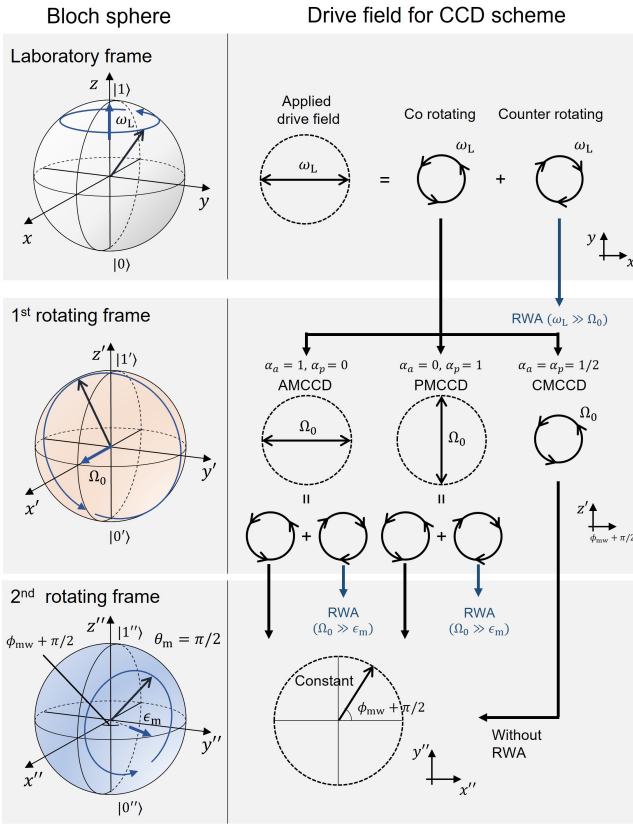


**FIG. 1. Polarization of drive field for different CCD schemes.** To control the qubit, a drive field resonant with the Larmor frequency  $\omega_L$  is applied. In most cases, the applied drive field is linearly polarized, which is a superposition of co and counter rotating circularly polarized fields. In the first rotating frame, the counter-rotating term results in a second harmonic field that can be neglected using RWA, since  $\Omega \ll \omega_L$ . For a pure amplitude or phase modulated drive, in the first rotating frame the modulation results in a linearly polarized field along x, y, respectively. In the second rotating frame, the RWA is not so valid as typically  $\epsilon_m < \Omega$ , and the counter-rotating term results in a systematic error in the gate. In this work, we propose CMCCD, where the amplitude and phase of the drive field are equally modulated, generating circular polarized field in the first rotating frame. Then in the second-rotating frame, there is no second-harmonic term reducing the gate error.

since  $\omega_L/2\pi = 10 - 20$  GHz  $\gg \Omega_0/2\pi = 1 - 10$  MHz. The second term represents standard Rabi drive field. Importantly, the detuning term is orthogonal to the Rabi drive field, which suppresses dephasing and contributes to the longer Rabi decay time  $T_2^{\text{Rabi}}$  than the dephasing time  $T_2^*$  [34]. The third term corresponds to the a.c. drive field generated by the CCD modulation. Notably, when  $\alpha_A = \alpha_P = 1/2$  (and zero Rabi error  $\Delta_\Omega = 0$ ), the drive field becomes circularly polarized (Fig. 1). Then we move to the second rotating frame defined by  $H_0^{(2)} = \frac{\Omega_0}{2} \sigma_{\phi_{\text{mw}}}$  as

$$\begin{aligned}
 H_{\text{rot}}^{(2)}(t) &= \frac{\Delta_\Omega}{2} \sigma_{\phi_{\text{mw}}} + \frac{\delta}{2} [\cos(\Omega_0 t) \sigma_z + \sin(\Omega_0 t) \sigma_{\phi_{\text{mw}} + \pi/2}] && \text{(Error terms)} \\
 &+ \left[ \alpha_P + \left( 1 + \frac{\Delta_\Omega}{\Omega_0} \right) \alpha_A \right] \frac{\epsilon_m}{2} [\cos(\theta_m) \sigma_z + \sin(\theta_m) \sigma_{\phi_{\text{mw}} + \pi/2}] && \text{(Co-rotating term)} \\
 &+ \left[ \alpha_P - \left( 1 + \frac{\Delta_\Omega}{\Omega_0} \right) \alpha_A \right] \frac{\epsilon_m}{2} [\cos(2\Omega_0 t - \theta_m) \sigma_z + \sin(2\Omega_0 t - \theta_m) \sigma_{\phi_{\text{mw}} + \pi/2}] && \text{(Counter-rotating term)} \quad (3)
 \end{aligned}$$

The first line represents Rabi and detuning errors. The

co-rotating term yields a d.c. drive field for the qubit

control at a frequency  $\epsilon_m/2\pi$ , which is orthogonal to the Rabi error term and parallel to the oscillating detuning error. If  $\epsilon_m \gg \Delta_\Omega$ , a Rabi error tilts the control field, resulting in a rotation error that is quadratic, rather than linear in the Rabi error. The oscillating detuning error modulates the precession frequency of the spin in the second rotating frame, leading to a phase shift that averages out to zero over time. The counter-rotating term is suppressed by RWA, which requires  $\epsilon_m \ll \Omega_0$ , and slow operations. For fast gates, the counter-rotating term results in a residual pulse-area error on resonance. However, by setting  $\alpha_P = \alpha_A$ , the counter-rotating term is cancelled and should lead to higher fidelity operations.

Figure 2 illustrates the time evolution of the qubit under various CCD schemes and the bare qubit. Here, we use modulation parameters as  $\epsilon_m = \Omega_0/4$ ,  $\theta_m = \pi/2$ , and  $\phi_{mw} = 0$ . The red lines on the Bloch spheres trace the trajectories of quantum states with blue dots exhibiting the points of each  $\pi/2$  pulse interval. First, we compare the trajectories between CCD schemes at zero detuning [Fig. 2(a)]. AMCCD and PMCCD schemes exhibit distorted trajectories and the plotted blue dots are spread even in the case of zero detuning. This distortion arises from the residual counter-rotating term. By contrast, CMCCD scheme, which eliminates counter-rotating terms, yields circular trajectories with accurately spaced  $\pi/2$  rotations, indicating precise qubit control. For the bare qubit, the trajectory remains circular. However, increasing detuning tilts the rotation axis, resulting in a spread of the blue dots and increased gate error. In CCD schemes, this spread is suppressed, thereby reducing error accumulation. Figure 2(b) illustrates the robustness of each scheme against Rabi errors. The bare qubit is highly sensitive to Rabi error, as indicated by widely spread blue dots. This sensitivity is substantially reduced in all CCD schemes, highlighting their effectiveness in suppressing amplitude-induced errors.

We further calculate the state infidelity for  $Y_\pi$  gate as a function of detuning and Rabi error (Fig. 3), using the same modulation parameters. For bare qubits, the infidelity increases significantly with detuning or Rabi error, whereas CCD-protected qubits demonstrate strong resilience to both error sources. While the degree of resilience varies among CCD implementations, CMCCD consistently achieves the highest gate fidelity in the low-error regime. This variation in error sensitivity across schemes can be attributed to differences in how effectively counter-rotating terms are suppressed. In particular, the asymmetric dependence on Rabi error observed in AMCCD and PMCCD arises from residual counter-rotating terms that are not entirely eliminated.

### III. DEVICE AND EXPERIMENTAL SETUP

To experimentally demonstrate the CCD scheme, we conduct our measurement on an isotopically purified silicon metal-oxide-semiconductor (SiMOS) quantum

dot [35]. The device consists of two quantum dots where single electron spin qubits are accumulated, and one single electron transistor (SET) for charge sensing (Fig 4). We readout the spin state via energy-selective tunneling [36], detected through the SET sensor. We apply static and pulsed voltages to the gates by voltage sources (QBLOX SPI D5a and Zurich Instruments HDAWG, respectively), while the SET current is measured using current-voltage amplifier (Basel SP983c) and monitored in real-time so that single electron tunneling event can be observed. The spin qubit manipulation is performed via the electron spin resonance (ESR), induced by MW through an aluminum antenna. The MW is generated by a MW source (Keysight PSG E8257D) and I/Q modulated by the signals from an arbitrary wave generator (Zurich Instruments HDAWG) to implement the CCD drive field. The device is cooled down to a base temperature of about 10 mK using a dilution refrigerator. Note that in this experiment, we use the electron spin-qubit confined in the left quantum dot (Q1).

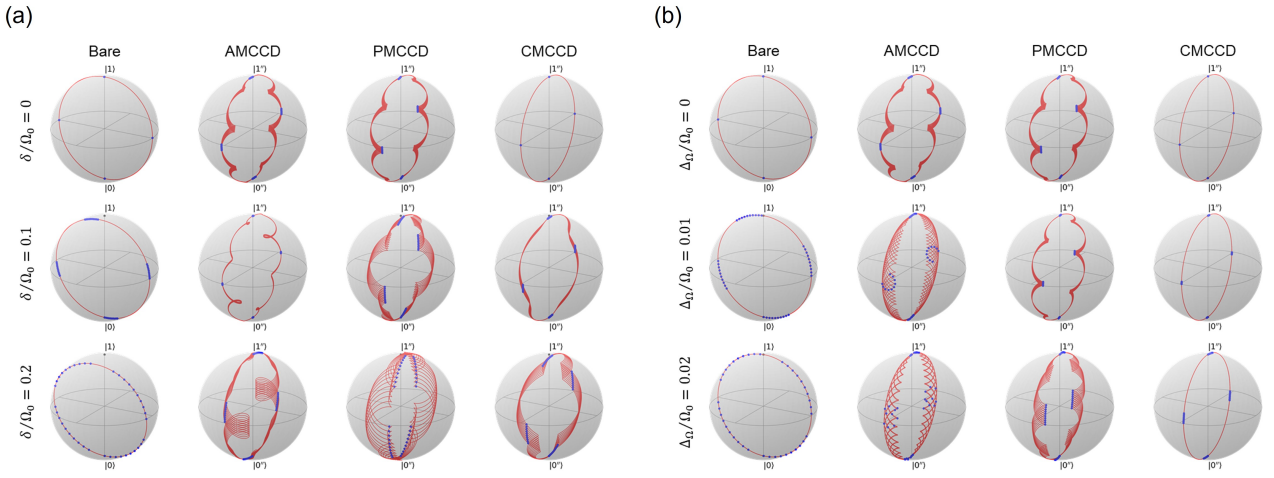


FIG. 2. Quantum state trajectories of the bare qubit and CCD-protected qubits under (a) detuning error and (b) Rabi error. Modulation parameters are set to  $\epsilon_m = \Omega_0/4$ ,  $\theta_m = \pi/2$ , and  $\phi_{mw} = 0$ . Red lines trace the evolution of the quantum states over a total rotation angle of  $20\pi$ , while blue markers indicate the positions corresponding to each  $\pi/2$  rotation interval. Note that Bloch spheres for CCD-protected qubits are shown in the second rotating frame, while that for the bare qubit is shown in the first rotating frame. For the case of zero detuning or Rabi error, the AMCCD and PMCCD give a spread in the rotations resulting from integer  $\pi/2$ -gates, whereas both the bare qubit and CMCCD give perfect integer  $\pi/2$ -gates. When a static error is introduced, all CCD schemes have a low spread in the state-vector at integer  $\pi/2$ -gates, whereas the bare qubit suffers a large spread in outcomes.

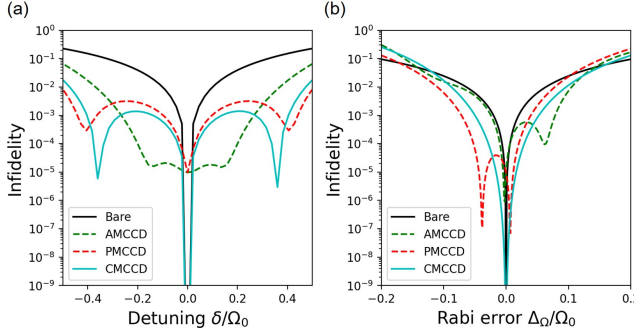


FIG. 3. Comparison of state infidelity for  $Y_\pi$  gate as a function of (a) detuning error and (b) Rabi error. Modulation parameters are set to  $\epsilon_m = \Omega_0/4$ ,  $\theta_m = \pi/2$ , and  $\phi_{mw} = 0$ . The  $Y_\pi$  gate performs  $Y$  axis rotation from  $|0''\rangle$  to  $|1''\rangle$  in the CCD schemes with a duration of  $\pi/\epsilon_m$ , and from  $|0'\rangle$  to  $|1'\rangle$  in the bare qubit with a duration of  $\pi/\Omega_0$ . The state infidelity is defined as  $1 - |\langle 1'' | Y_\pi | 0'' \rangle|^2$  for CCD schemes and  $1 - |\langle 1' | Y_\pi | 0' \rangle|^2$  for bare qubit. The CMCCD combines the accuracy of a bare Rabi gate at low error, with an improved tolerance to larger errors.

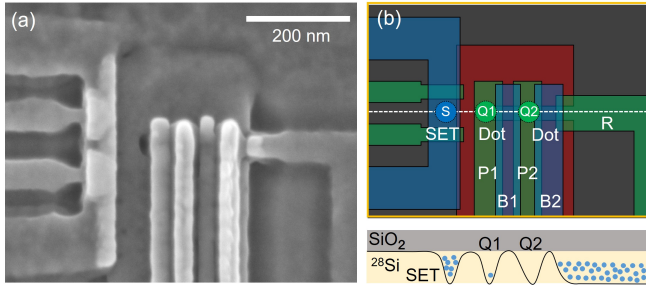


FIG. 4. (a) The top-view scanning electron microscope (SEM) image and (b) its schematic illustration, including a cross-section view along the white dashed line. We operate the electron spin-qubit confined in the left quantum dot (Q1).

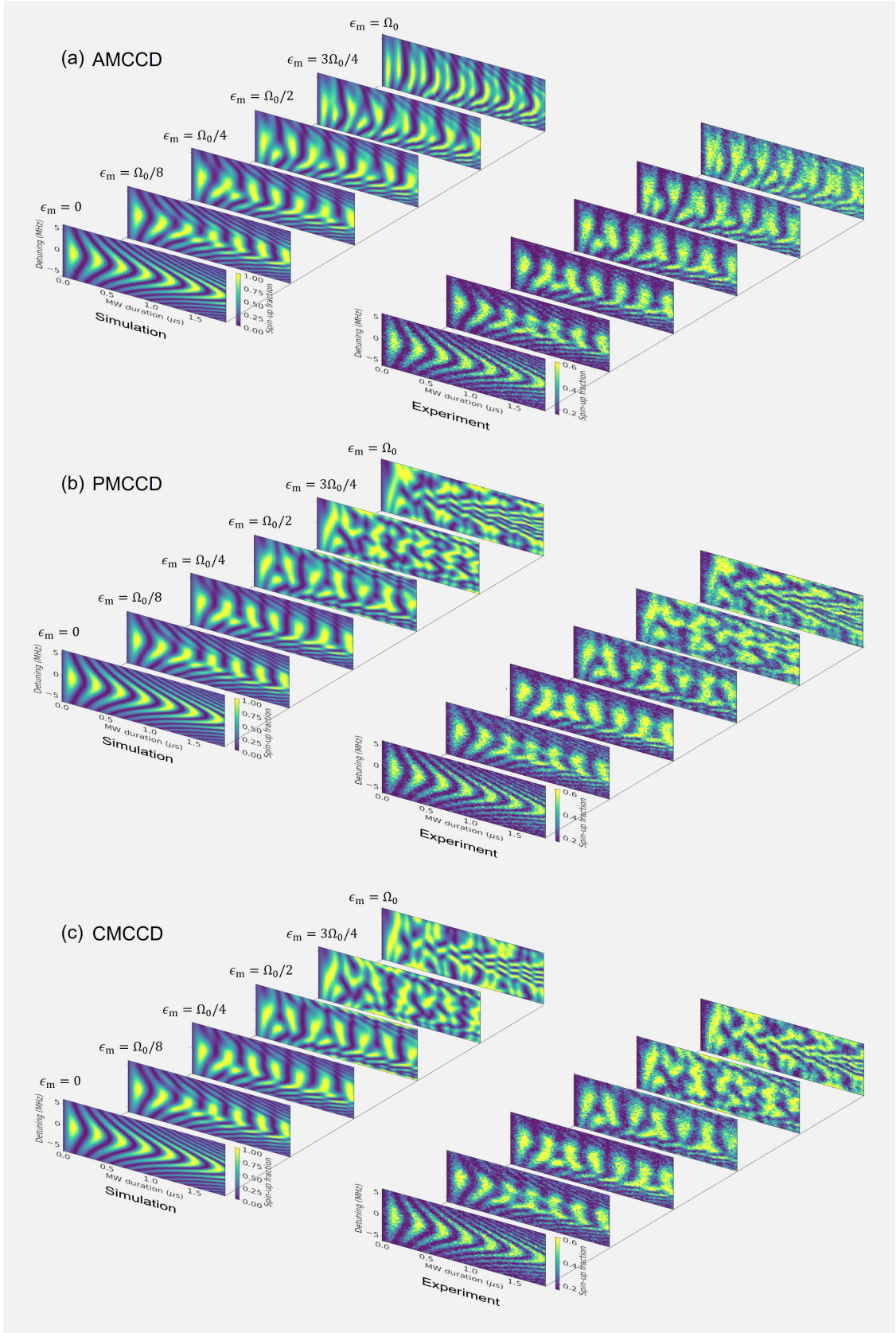


FIG. 5. Chevron pattern of different CCD schemes, (a) AMCCD, (b) PMCCD, and (c) CMCCD measured at  $\Omega_0 = 2\pi \times 3.6$  MHz. The left panels show the simulation, and the right panels show the corresponding experimental results. We measure the chevron pattern by varying the  $\epsilon_m$  from 0 to  $\Omega_0$ . When  $\epsilon_m = 0$ , the condition is the same as the bare qubit. As  $\epsilon_m$  increases, the chevron pattern gradually transforms into a ladder-like structure, indicating enhanced robustness against detuning. With further increase toward  $\Omega_0$ , the ladder-like shape begins to distort, and the robustness correspondingly decreases.

#### IV. PROPERTIES OF STABILIZED RABI OSCILLATION

In this section, we investigate the properties of stabilized Rabi oscillation by different CCD schemes. As explained in the previous section, the CCD scheme can improve the robustness of both detuning error and Rabi error. Firstly, to demonstrate the amplitude-phase modulated CCD, we show simulation and experimental results of Rabi oscillations over the detuning in Fig. 5. We measure the Rabi oscillations by three types of CCD schemes at the bare qubit Rabi frequency  $\Omega_0/2\pi = 3.6$  MHz. From the usual Rabi chevron pattern ( $\epsilon_m = 0$ ), as increasing  $\epsilon_m$ , the chevron pattern is modified and becomes a more complex pattern. When  $\epsilon_m$  is small, there is almost no difference in the maps between the three CCD schemes, but as  $\epsilon_m$  increases, the difference becomes more pronounced. Simulation and experimental results are in good agreement, demonstrating the proper implementation of the amplitude-phase modulated CCD schemes. Note that the slight difference between the simulation and experimental results of AMCCD [Fig. 5(a)] for large  $\epsilon_m$  is due to the nonlinearity of the MW amplifier.

For the bare qubit with a detuning  $\delta$ , the spin rotates about a tilted axis at the oscillation frequency as  $\sqrt{\Omega_0^2 + \delta^2}$ , revealing the usual chevron pattern [Fig. 6(a)]. In the CCD schemes, the qubit is rotating about two axes for executing the dynamic decoupling, decreasing the sensitivity to the detuning error. The Rabi oscillations over the detuning in CCD schemes exhibit an improvement in robustness against the detuning error. The chevron patterns of the bare qubit is changed to ladder-like structures as shown in Fig. 6(b)-(d). The CCD's robustness against the detuning is also clearly evident in the Fourier spectrums. In contrast to the hyperbolic dependence of the detuning for the bare qubit, the spectrums in CCD schemes are flat in a certain range of the detuning. For silicon spin qubits, the detuning error varies in time due to fluctuations of nuclear spins from  $^{29}\text{Si}$  isotopes [37–39]. In addition, when manipulating multi-qubits, variations in the  $g$ -factor cause differences in the resonance frequency between the qubits [40, 41], resulting in detuning errors. These results show that CCD schemes can perform qubit operations that are robust against variations in the detuning.

Next, we investigate robustness against the Rabi error, which is caused by the fluctuations in the qubit drive field. In particular, when considering the multiple silicon spin qubits, the Rabi error can also arise from variations in the  $g$ -factor and the spatial inhomogeneity of the MW. In this experiment, we artificially increase or decrease the MW amplitude and evaluate the robustness against a static Rabi error. Figures 7(a)-(d) show the simulation and experimental results of Rabi oscillations over the Rabi error. For the bare qubit, as the Rabi error increases, the Rabi frequency becomes higher, and this is expressed by the linear dependence of the Fourier

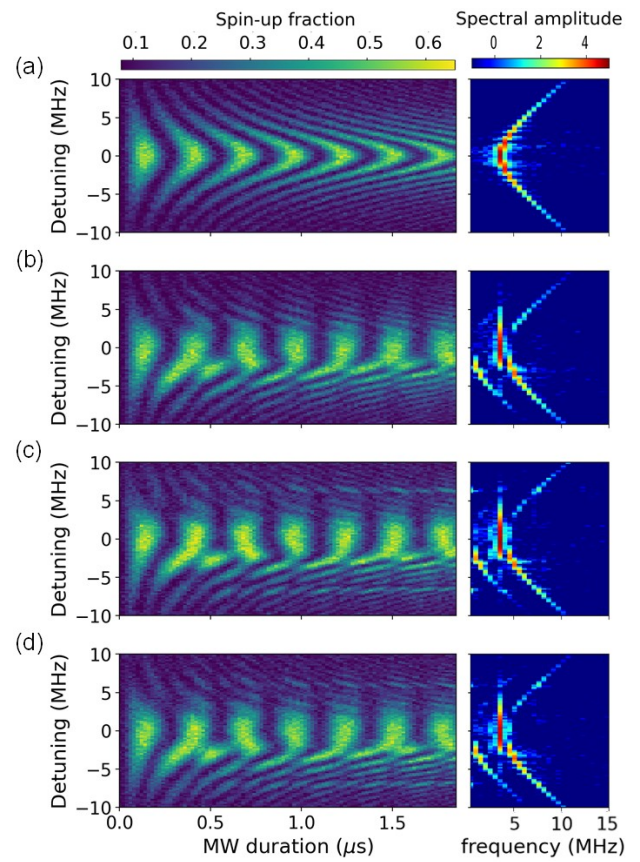
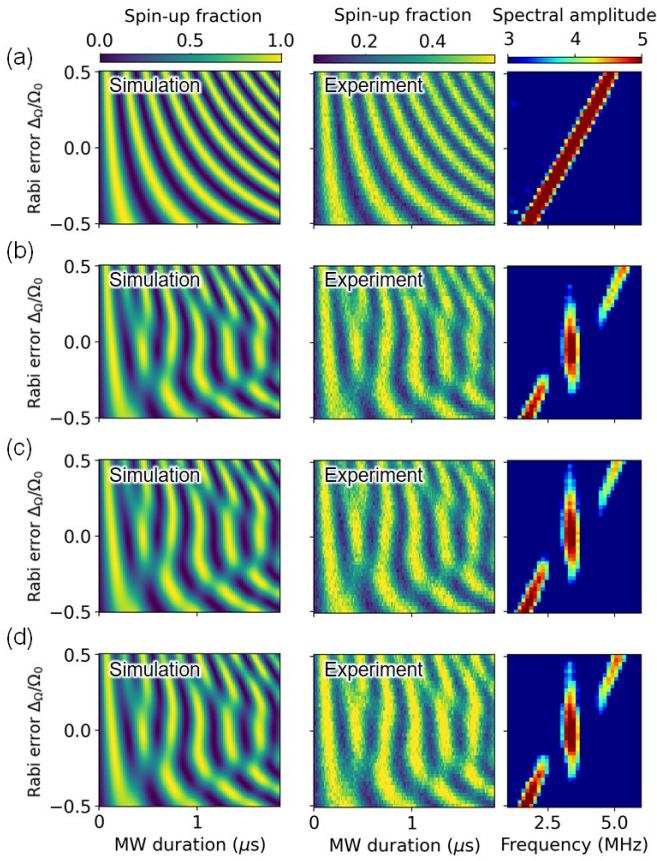


FIG. 6. **Comparison of Rabi chevrons** (Spin up fraction following drive vs duration and detuning of the drive (left panels), and their Fourier transform (right panels)). (a) Bare qubit, (b) AMCCD, (c) PMCCD and (d) CMCCD. We measure the chevron patterns under the same conditions, where  $\Omega_0 = 2\pi \times 3.6$  MHz for the bare qubit, and  $\epsilon_m = \Omega_0/4 = 2\pi \times 0.9$  MHz for the CCD schemes. The bare qubit exhibits a classic chevron pattern with an effective Rabi frequency that has hyperbolic dependence on detuning. The CCD patterns have a ladder-like structure. In the Fourier domain, near zero detuning there is a single frequency component at the modulation frequency, which is robust against detuning errors.

spectrum [Fig. 7(a)]. This linear dependence shows that the bare qubit is vulnerable to the Rabi error. By applying CCD schemes, within a range of around  $\pm 20\%$  of the Rabi error, the obtained Rabi frequency is insensitive to the Rabi error as shown in Figs. 7(b)-(d). These maps of Rabi error dependence of Rabi oscillations are in excellent agreement with those predicted from simulations.

From the above examinations, we demonstrate that CCD schemes are resistant to detuning and Rabi errors. Furthermore, we confirm that the proposed CMCCD achieves the same effect as the conventional single amplitude/phase modulation CCD and is consistent with the simulation. In the next section, we will evaluate the performance of the gate fidelity for CCD qubits via randomized benchmarking method.



**FIG. 7. Sensitivity of CCD to static Rabi errors.** Dependence of Rabi oscillations on static Rabi errors measured at  $\Omega_0 = 2\pi \times 3.3$  MHz for the bare qubit, and  $\epsilon_m = \Omega_0/4 = 2\pi \times 0.825$  MHz for the CCD schemes. (a) Bare qubit, (b) AMCCD, (c) PMCCD and (d) CMCCD. The left panels show simulation results. The middle panels are experimental results, showing excellent agreement with simulations. The right panels show the Fourier spectrums over the MW duration time. The bare qubit has a linear dependence of the Rabi frequency on the Rabi error. By applying the CCD scheme, the Rabi frequency becomes constant within a certain range of Rabi errors, as can be seen from the Fourier spectrums, showing the reduction in the sensitivity to Rabi error.

At the end of this section, we examine the characteristics of the CCD schemes for Rabi oscillations with no artificial errors. Figures 8(a) and (b) show Rabi frequency  $\Omega_0/2\pi$  dependence of Rabi oscillation decay time  $T_2^{\text{Rabi}}$  and quality factor  $Q$ . Here, we define  $Q$  as the decay time  $T_2^{\text{Rabi}}$  divided by the  $\pi$  rotation time  $T_\pi$ ,  $Q = T_2^{\text{Rabi}}/T_\pi$ . We use  $\epsilon_m = \Omega_0/4$  for CCD schemes and extract the decay time  $T_2^{\text{Rabi}}$  by fitting to an exponentially decaying sinusoidal. For comparison, we plot the bare qubit results. As shown in Fig. 8(a), the decay time  $T_2^{\text{Rabi}}$  decreases as  $\Omega_0/2\pi$  increases. This decrease is probably due to the MW induced noise observed in the ESR or ESDR experiments [42]. The maximum  $Q$  of the bare qubit is about 70, but this value is almost similar to those of three CCD schemes as shown in Fig. 8(b). To further

investigate the CCD schemes, we plot the quality factor  $Q$  as a function of modulation strength  $\epsilon_m$  [Fig. 8(c)]. When  $\epsilon_m$  is small, no significant differences are observed between the CCD schemes, but as  $\epsilon_m/\Omega_0$  approaches 1,  $Q$  decreases in AMCCD and CMCCD. This behavior is probably attributed to the MW induced noise caused by an increase in  $\epsilon_m$  of CCD schemes that include amplitude modulation. We note here that the CCD schemes cannot improve the quality  $Q$ , unlike the previous reports from using a natural silicon quantum dot [33]. This fact indicates that the dominant noise source limiting  $Q$  in this experimental system is the high-frequency noise, which cannot be removed by the CCD schemes.

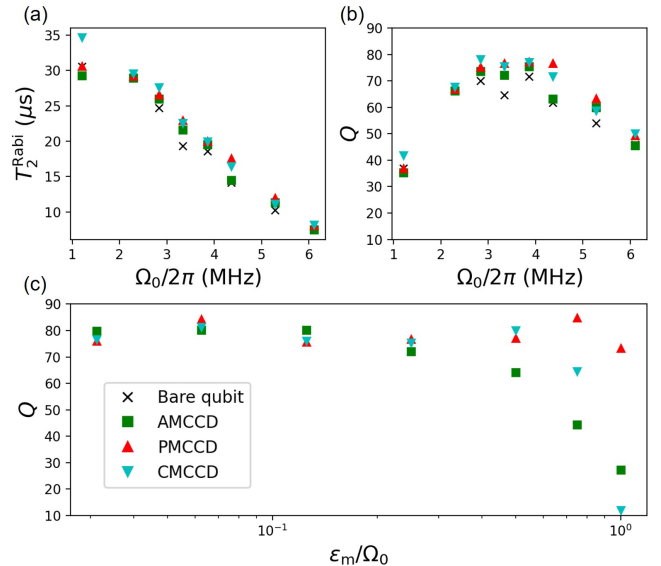


**FIG. 8. Properties of Rabi oscillations without the artificial error.** (a)  $\Omega_0/2\pi$  dependence of  $T_2^{\text{Rabi}}$ .  $T_2^{\text{Rabi}}$  decreases as the  $\Omega_0/2\pi$  increases due to the increase in the heating from the MW pulse. (b)  $\Omega_0/2\pi$  dependence of quality factor  $Q$ . No significant improvement is found by using CCD schemes. (c)  $\epsilon_m$  dependence of quality factor  $Q$  measured at  $\Omega_0 = 2\pi \times 3.6$  MHz. In PMCCD, there is no significant dependence on  $\epsilon_m$ . In AMCCD and CMCCD, increasing  $\epsilon_m$  decreases  $Q$  due to the MW induced noise caused by the amplitude modulation.

## V. CHARACTERISTICS OF CCD-PROTECTED QUBIT

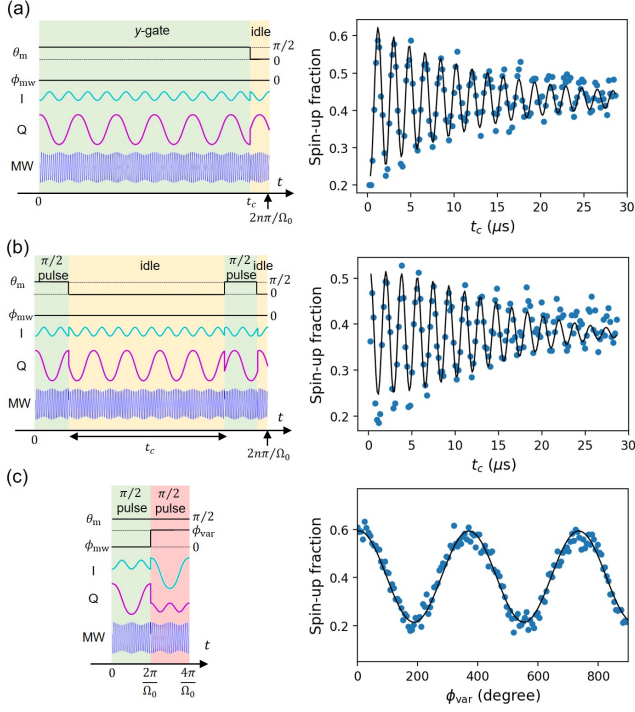


FIG. 9. **Control of the double dressed qubit by CMCCD scheme.** The left schematics of each figure show the pulse sequences. All experiments are measured at  $\Omega_0 = 2\pi \times 2.2$  MHz and  $\epsilon_m = \Omega_0/4$ . (a) CCD-Rabi experiment. The first pulse executes  $y$ -axis rotation of  $t_c$  duration. The second pulse is an idle pulse to adjust the readout time to  $2n\pi/\Omega_0$ . This matches the laboratory and the second rotating frame basis for readout [33]. The decay time  $T_2^{\text{CCD-Rabi}} = 12.8 \mu\text{s}$ . (b) CCD-Ramsey experiment. The idle pulse of duration  $t_c$  is applied between two  $\pi/2$  pulses, followed by the idle pulse for the readout matching. The decay time  $T_2^{\text{CCD-Ramsey}} = 17.7 \mu\text{s}$ . (c) Two-axis control experiment. We apply two consecutive  $\pi/2$  pulses and vary the MW phase  $\phi_{\text{var}}$ . The spin-up probability as a function of  $\phi_{\text{var}}$  oscillates with a period of  $2\pi$ , demonstrating the control of the rotation axis in the double dressed qubit by CMCCD.

In the previous section, we focused on the Rabi oscillations in the first rotating frame. This section examines the CCD-protected qubit defined in the double dressed state. To take advantage of the robustness provided by CCD schemes, we need to control the CCD-protected qubit defined in the second rotating frame. The readout and control method of the CCD-protected qubit was discussed in ref [33]. In this study, we first confirm the qubit control using the CMCCD scheme. As described in Eq. (3), we achieve  $z$  rotation by setting  $\theta_m = 0$  for idle pulse, and  $x$ - $y$  plane axis rotation for the gate operation by setting  $\theta_m = \pi/2$ , varying the rotation axis with  $\phi_{\text{mw}}$ . Figures 9(a)-(c) show basic control pulse sequences and experimental results. As shown in Fig. 9(a), to demon-

strate the  $y$ -gate operation, we apply pulse duration of  $t_c$ , where  $\theta_m = \pi/2$  and  $\phi_{\text{mw}} = 0$ , followed by the idle pulse for readout matching. We observe the Rabi oscillation in the second rotating frame at the frequency of  $\epsilon_m/2\pi$  as expected. Next, we measure the coherence time of the double dressed qubit by CMCCD scheme as shown in Fig 9(b). The observed oscillations correspond to the  $z$  rotation of the idle pulse. In the experiments, we evaluate the decay times by fitting to a decaying exponential and obtain  $T_2^{\text{CCD-Rabi}} = 12.8 \mu\text{s}$  and  $T_2^{\text{CCD-Ramsey}} = 17.7 \mu\text{s}$ . In Fig. 9(c), we then demonstrate the two-axis control by the MW phase  $\phi_{\text{mw}}$ . After a  $\pi/2$  pulse of the MW phase  $\phi_{\text{mw}} = 0$ , we apply the additional  $\pi/2$  pulse, varying the MW phase of  $\phi_{\text{mw}} = \phi_{\text{var}}$ . The obtained spin-up fraction oscillates with a period of  $2\pi$ , thus achieving the two-axis control in the CMCCD scheme.

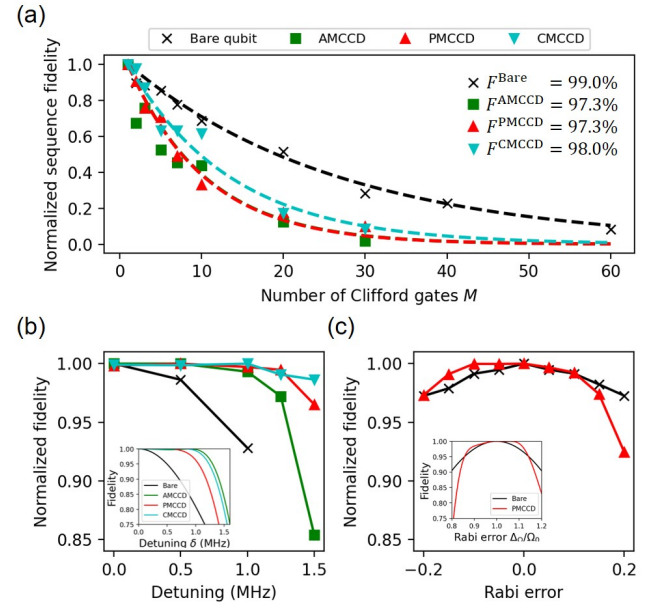


FIG. 10. **Robustness of gate fidelity using randomized benchmarking.** Experiments are conducted at  $\Omega_0 = 2\pi \times 2.2$  MHz and  $\epsilon_m = \Omega_0/4$ . (a) Randomized benchmarking of the bare qubit and CCD qubits. The sequence is repeated for  $K=15$  random Clifford gate sets. The normalized gate fidelity as a function of (b) detuning and (c) Rabi error. For comparison, we put insets showing the simulation results of  $Y_\pi$  gate state fidelity, the same data as in Fig.3.

Finally, we investigate the gate fidelity and the robustness of three CCD schemes and compare them with the bare qubit. Figure 10(a) shows the reference randomized benchmarking measurement data to determine the average single gate fidelity [43, 44]. In this sequence,  $M$  random Clifford gates are applied, followed by a recovery Clifford gate that returns the final spin state to spin-up or spin-down. We plot the differences in spin-up fraction between two cases and fit the data to an exponential curve of the form  $(2F_c - 1)^M$ . From this fit, we extract the average Clifford gate fidelity  $F_c$ . The fidelity of an average

single gate, denoted as  $F$ , is then calculated using the relation:  $F = 1 - (1 - F_c)/1.875$  [44]. In the following experiments, for CCD schemes, we use the modulation strength  $\epsilon_m = \Omega_0/4$  to minimize the counter-rotating term appeared in AMCCD and PMCCD scheme [33]. It can be seen that the fidelity is lower with CCD schemes compared to bare qubit. As can be inferred from the results in the previous section, the dominant noise in this experimental system cannot be removed by the CCD, so the fidelity is reduced simply by slowing the gate speed by a factor of 4 ( $\epsilon_m = \Omega_0/4$ ). On the other hand, the CCD scheme can improve robustness against the detuning and the Rabi errors. To characterize the robustness of CCD qubits, we artificially apply static detuning or Rabi error and evaluate the gate fidelity. Figure 10(b) shows the measured gate fidelity as a function of detuning. The fidelity of the bare qubit decreases as detuning increases, whereas CCD qubits show a decrease in sensitivity to detuning, enabling the fidelity to be maintained even under some detuning. Figure 10(c) presents the Rabi error dependence of the fidelity. The effect of PMCCD is particularly evident in the Rabi error  $\Delta_\Omega/\Omega_0$  range of -0.15 to 0 [Fig. 10(c)]. However, the improvement in robustness against Rabi errors is not as significant as that against detuning errors. This is because CCD qubits have a double dynamical decoupling effect against detuning errors, introduced by the two frame transforms. Note that as shown in Fig. 3(b), simulations suggest that PMCCD, which operates without amplitude modulation, offers better robustness to Rabi errors and allows easier experimental comparison. Based on this, we used PMCCD to study the effect of Rabi error.

## VI. SUMMARY

In this study, we explore the implementation of the CCD scheme for qubit applications. A limitation of the conventional CCD scheme lies in the RWA in the second rotating frame, which can degrade the gate fidelity. To address this issue, we propose the CMCCD scheme, which employs dual modulation of MW amplitude and phase for qubit driving. This approach eliminates the residual counter-rotating term and dynamically decouples qubits from noise, thereby obviating the need for RWA.

We experimentally implement the CMCCD scheme using an electron spin-qubit in an isotopically purified silicon quantum dot. The dependence of the chevron pattern on the CCD modulation strength  $\epsilon_m$  aligns well with simulation results, confirming the accurate implementation of the proposed scheme. We further assess the robustness against detuning and Rabi errors by measuring Rabi oscillations and their Fourier spectrum over MW duration. Our findings indicate a significant improvement in robustness compared to bare qubits, consistent with simulation predictions. Moreover, this enhanced robustness extends to CCD qubits defined in the double-

dressed state. We evaluate the effectiveness of the CCD schemes by measuring gate fidelity through randomized benchmarking under artificially induced errors. The robustness is significantly improved with CCD schemes, demonstrating advantages for stable qubit control under imperfect and noisy conditions. We note that while the robustness is improved, the base gate fidelity is not improved using the CCD schemes, unlike the previous study in a natural silicon device with higher low frequency noise [33]. This fact suggests that the dominant noise in this experiment is high-frequency noise that cannot be canceled by CCD schemes, and thereby no significant improvement can be seen for the proposed CMCCD. To achieve high fidelity gate operations with the proposed CMCCD scheme, further evaluation under environments with reduced high-frequency noise remains an important direction for future work.

The CCD scheme presents a valuable tool for controlling qubits in noisy environments and under variations in qubit characteristics or driving fields. This method provides reliable control strategies indispensable for multi-qubit systems in fault-tolerant quantum computers. Furthermore, as the proposed CMCCD scheme does not require RWA, it is anticipated to enable higher fidelity gate operations applicable not only to silicon spin-qubits but also other types of qubits, such as trapped atoms [45], cold atoms [46], superconducting qubits, and NV-centers [24].

## ACKNOWLEDGEMENT

This work was supported by JST Moonshot R & D Grant No. JPMJM2065.

\* takuma.kuno.pg@hitachi.com

[1] C. L. Degen, F. Reinhard, and P. Cappellaro, *Rev. Mod. Phys.* **89**, 035002 (2017).

[2] D. DeMille, N. R. Hutzler, A. M. Rey, and T. Zelevinsky, *Nat. Phys.* **20**, 741 (2024).

[3] V. Giovannetti, S. Lloyd, and L. Maccone, *Phys. Rev. Lett.* **96**, 010401 (2006).

[4] R. P. Feynman, *Int. J. Theor. Phys.* **21** (1982).

[5] I. M. Georgescu, S. Ashhab, and F. Nori, *Rev. Mod. Phys.* **86**, 153 (2014).

[6] T. Hensgens, T. Fujita, L. Janssen, X. Li, C. J. Van Diepen, C. Reichl, W. Wegscheider, S. Das Sarma, and L. M. K. Vandersypen, *Nature* **548**, 70 (2017).

[7] D. P. DiVincenzo, *Fortschr. Phys.* **48**, 771 (2000).

[8] M. A. Nielsen and I. L. Chuang, *Quantum computation and quantum information* (Cambridge University Press, 2010).

[9] R. Raussendorf and J. Harrington, *Phys. Rev. Lett.* **98**, 190504 (2007).

[10] A. G. Fowler, M. Mariantoni, J. M. Martinis, and A. N. Cleland, *Phys. Rev. A* **86**, 032324 (2012).

[11] J. Preskill, *Quantum* **2**, 79 (2018).

[12] N. Timoney, I. Baumgart, M. Johanning, A. F. Varón, M. B. Plenio, A. Retzker, and C. Wunderlich, *Nature* **476**, 185 (2011).

[13] R. Bowler and D. Leibfried, *Phys. Rev. Lett.* **110**, 263002 (2013).

[14] X. Xu, Z. Wang, C. Duan, P. Huang, P. Wang, Y. Wang, N. Xu, X. Kong, F. Shi, X. Rong, *et al.*, *Phys. Rev. Lett.* **109**, 070502 (2012).

[15] D. A. Golter, T. K. Baldwin, and H. Wang, *Phys. Rev. Lett.* **113**, 237601 (2014).

[16] H. Morishita, T. Tashima, D. Mima, H. Kato, T. Makino, S. Yamasaki, M. Fujiwara, and N. Mizuuchi, *Sci. Rep.* **9**, 13318 (2019).

[17] K. C. Miao, J. P. Blanton, C. P. Anderson, A. Bourassa, A. L. Crook, G. Wolfowicz, H. Abe, T. Ohshima, and D. D. Awschalom, *Science* **369**, 1493 (2020).

[18] A. Laucht, R. Kalra, S. Simmons, J. P. Dehollain, J. T. Muhonen, F. A. Mohiyaddin, S. Freer, F. E. Hudson, K. M. Itoh, D. N. Jamieson, *et al.*, *Nat. Nanotechnol.* **12**, 61 (2017).

[19] K. Tsoukalas, U. von Lüpke, A. Orekhov, B. Hetényi, I. Seidler, L. Sommer, E. G. Kelly, L. Massai, M. Aldeghi, M. Pita-Vidal, *et al.*, *arXiv* (2025), 2501.14627.

[20] I. Hansen, A. E. Seedhouse, A. Saraiva, A. Laucht, A. S. Dzurak, and C. H. Yang, *Phys. Rev. A* **104**, 062415 (2021).

[21] H. H. Vallabhapurapu, I. Hansen, C. Adambukulam, R. Stöhr, A. Denisenko, C. H. Yang, and A. Laucht, *Phys. Rev. A* **108**, 022606 (2023).

[22] I. Hansen, A. E. Seedhouse, K. W. Chan, F. E. Hudson, K. M. Itoh, A. Laucht, A. Saraiva, C. H. Yang, and A. S. Dzurak, *Appl. Phys. Rev.* **9** (2022).

[23] I. Hansen, A. E. Seedhouse, S. Serrano, A. Nickl, M. Feng, J. Y. Huang, T. Tanttu, N. Dumoulin Stuyck, W. H. Lim, F. E. Hudson, *et al.*, *Nat. Commun.* **15**, 7656 (2024).

[24] J. M. Cai, B. Naydenov, R. Pfeiffer, L. P. McGuinness, K. D. Jahnke, F. Jelezko, M. B. Plenio, and A. Retzker, *New J. Phys.* **14**, 113023 (2012).

[25] I. Cohen, N. Aharon, and A. Retzker, *Fortschr. Phys.* **65**, 1600071 (2017).

[26] A. Stark, N. Aharon, T. Unden, D. Louzon, A. Huck, A. Retzker, U. L. Andersen, and F. Jelezko, *Nat. Commun.* **8**, 1105 (2017).

[27] D. Farfurnik, N. Aharon, I. Cohen, Y. Hovav, A. Retzker, and N. Bar-Gill, *Phys. Rev. A* **96**, 013850 (2017).

[28] G. Wang, Y.-X. Liu, and P. Cappellaro, *New J. Phys.* **22**, 123045 (2020).

[29] Q.-Y. Cao, P.-C. Yang, M.-S. Gong, M. Yu, A. Retzker, M. B. Plenio, C. Müller, N. Tomek, B. Naydenov, L. P. McGuinness, *et al.*, *Phys. Rev. Appl.* **13**, 024021 (2020).

[30] G. Wang, Y.-X. Liu, and P. Cappellaro, *Phys. Rev. A* **103**, 022415 (2021).

[31] A. Salhov, Q. Cao, J. Cai, A. Retzker, F. Jelezko, and G. Genov, *Phys. Rev. Lett.* **132**, 223601 (2024).

[32] A. J. Ramsay, R. Hekmati, C. J. Patrickson, S. Baber, D. R. M. Arvidsson-Shukur, A. J. Bennett, and I. J. Luxmoore, *Nat. Commun.* **14**, 461 (2023).

[33] T. Kuno, T. Utsugi, A. J. Ramsay, N. Mertig, N. Lee, I. Yanagi, T. Mine, N. Kusuno, R. Mizokuchi, T. Nakajima, *et al.*, *arXiv* (2025), 2503.19410.

[34] P. Stano and D. Loss, *Nat. Rev. Phys.* **4**, 672 (2022).

[35] A. Elsayed, M. M. K. Shehata, C. Godfrin, S. Kubicek, S. Massar, Y. Canvel, J. Jussot, G. Simion, M. Mongillo, D. Wan, *et al.*, *npj Quantum Inf.* **10**, 70 (2024).

[36] J. M. Elzerman, R. Hanson, L. H. Willems van Beveren, B. Witkamp, L. M. K. Vandersypen, and L. P. Kouwenhoven, *Nature* **430**, 431 (2004).

[37] A. V. Khaetskii, D. Loss, and L. Glazman, *Phys. Rev. Lett.* **88**, 186802 (2002).

[38] R. Hanson, L. P. Kouwenhoven, J. R. Petta, S. Tarucha, and L. M. K. Vandersypen, *Rev. Mod. Phys.* **79**, 1217 (2007).

[39] L. V. C. Assali, H. M. Petrilli, R. B. Capaz, B. Koiller, X. Hu, and S. Das Sarma, *Phys. Rev. B* **83**, 165301 (2011).

[40] R. Ferdous, K. W. Chan, M. Veldhorst, J. C. C. Hwang, C. H. Yang, H. Sahasrabudhe, G. Klimeck, A. Morello, A. S. Dzurak, and R. Rahman, *Phys. Rev. B* **97**, 241401 (2018).

[41] J. D. Cifuentes, T. Tanttu, W. Gilbert, J. Y. Huang, E. Vahapoglu, R. C. C. Leon, S. Serrano, D. Otter, D. Dunmore, P. Y. Mai, *et al.*, *Nat. Commun.* **15**, 4299 (2024).

[42] B. Undseth, O. Pietx-Casas, E. Raymenants, M. Mehmandoost, M. T. Madzik, S. G. J. Philips, S. L. De Snoo, D. J. Michalak, S. V. Amitonov, L. Tryputen, *et al.*, *Phys. Rev. X* **13**, 041015 (2023).

[43] E. Knill, D. Leibfried, R. Reichle, J. Britton, R. B. Blakestad, J. D. Jost, C. Langer, R. Ozeri, S. Seidelin, and D. J. Wineland, *Phys. Rev. A* **77**, 012307 (2008).

[44] J. T. Muhonen, A. Laucht, S. Simmons, J. P. Dehollain, R. Kalra, F. E. Hudson, S. Freer, K. M. Itoh, D. N. Jamieson, J. C. McCallum, *et al.*, *J. Phys.: Condens. Matter* **27**, 154205 (2015).

[45] M. Nünnerich, D. Cohen, P. Barthel, P. H. Huber, D. Niroomand, A. Retzker, and C. Wunderlich, *Phys. Rev. X* **15**, 021079 (2025).

[46] G. Wang, W. Xu, C. Li, V. Vuletić, and P. Cappellaro, *Phys. Rev. Appl.* **23**, 024072 (2025).